A proxy for magmatic foams: FOAMGLAS®, a closed-cell glass insulation

Amy Ryan, Stephan Kolzenburg, Alessandro Vona, Michael Heap, James Russell, Steven Badger

Journal of Non-Crystalline Solids: X 1 (2019) 100001

Contents lists available at ScienceDirect

Journal of Non-Crystalline Solids: X

journal homepage: www.journals.elsevier.com/journal-of-non-crystalline-solids-x

A proxy for magmatic foams: FOAMGLAS®, a closed-cell glass insulation

Amy G. Ryan[a,*], Stephan Kolzenburg[b,c], Alessandro Vona[d], Michael J. Heap[e], James K. Russell[a], Steven Badger[f]

[a] Volcanology and Petrology Laboratory, EOAS, University of British Columbia, 2020-2207 Main Mall, Vancouver, BC V6T 1Z4, Canada
[b] Department of Earth and Planetary Sciences, McGill University, 3450 University Street, Montreal, QC H3A 0E8, Canada
[c] Department für Geo- und Umweltwissenschaften, Ludwig-Maximilians-Universität. 80333 München, Germany
[d] Dipartimento di Scienze, Università degli Studi Roma Tre, L.go San Leonardo Murialdo 1, 00146 Roma, Italy
[e] Institut de Physique de Globe de Strasbourg (UMR 7516 CNRS, Université de Strasbourg/EOST), 5 rue René Descartes, 67084 Strasbourg, France
[f] Owens Corning Corporation, 1 Owens Corning Parkway, Toledo, OH 43659, United States

ARTICLE INFO

Keywords:
Experiment
Volcanology
Rheology
Porosity
Strain-hardening
Permeability

ABSTRACT

FOAMGLAS® is a closed-cell glass insulation that has a high porosity, is impermeable, and can be heated above its glass transition temperature (*Tg*) without fracturing. Here, we characterize, using standard laboratory techniques, the thermal and transport properties of FOAMGLAS®, and report viscometry and calorimetry results. Based on this characterization, we propose that FOAMGLAS® be used as a proxy material in studies of the deformational behaviour of natural crystal-free melts populated with isolated bubbles. We demonstrate its utility with a case study: cores of FOAMGLAS® are deformed at high temperature (> *Tg*) in uniaxial compression. Deformed FOAMGLAS® samples record a different pattern of strain accumulation (volume loss vs. bulging) compared to deformed natural materials where bubble connectivity is high (e.g., sintered ash, vesicular lavas). The divergent behaviour can be ascribed to pressurization of the isolated gas-filled bubbles as a result of compression. The pressurized bubbles resist deformation, and expand when unloaded. In contrast, the high connectivity of open-cell foams allows gas escape and collapse of pore space during compression. The different behaviours of open- and closed-cell melt foams highlight the influence of isolated bubbles on magma rheology. These results demonstrate the utility of FOAMGLAS® as an experimental analogue for closed-cell bubble-rich magmas.

1. Introduction

In magmatic and volcanic systems, ascending silicate melts foam as they transit the Earth to erupt. Foaming produces melt populated with gas-filled bubbles. Empirically, we know the addition of bubbles to a melt has a large impact on magma density [1], thermal diffusivity and conductivity [2], viscosity [3–6], and the potential for fragmentation [7]. However, a quantitative understanding of how bubble content affects the bulk properties of bubble-rich melts is mainly absent. In the geological sciences, we often design experiments to produce data that inform on the effects of bubbles to fill existing gaps in our understanding [2–4,8]. A critical element for ensuring the experimental results are widely applicable is using a well-characterized starting material (i.e. materials for which the glass water content, average bubble size, bubble size distribution, etc. are already known). Here we propose FOAMGLAS®, a cellular glass insulation, as an analogue for bubble-rich melts in experimental studies conducted above the glass transition temperature (*Tg*). In the following sections we characterize the material and demonstrate its utility in experimental studies of magmatic foams.

2. FOAMGLAS®

FOAMGLAS® is a high-porosity cellular glass insulation produced by Owens Corning Corporation [9]. It is a durable low-density industrial material, favoured for its high compressive strength (given its porosity) and low thermal conductivity. It is impermeable to water and water vapour. Many of the physical and thermal properties, which have been determined using ASTM (American Society for Testing and Materials) methods and standards, are reported by Owens Corning for each of the materials within the FOAMGLAS® product line [10].

FOAMGLAS® HLB 2400, the specific FOAMGLAS® product used throughout this study, is synthesized from recycled soda-lime glass and other natural materials, including sand, dolomite, and lime. No fibres or binders are present in the material [11]. The bubbles in the glass foam

* Corresponding author.
E-mail address: aryan@eoas.ubc.ca (A.G. Ryan).

https://doi.org/10.1016/j.nocx.2018.100001
Received 27 September 2018; Received in revised form 21 November 2018; Accepted 27 November 2018
Available online 10 December 2018

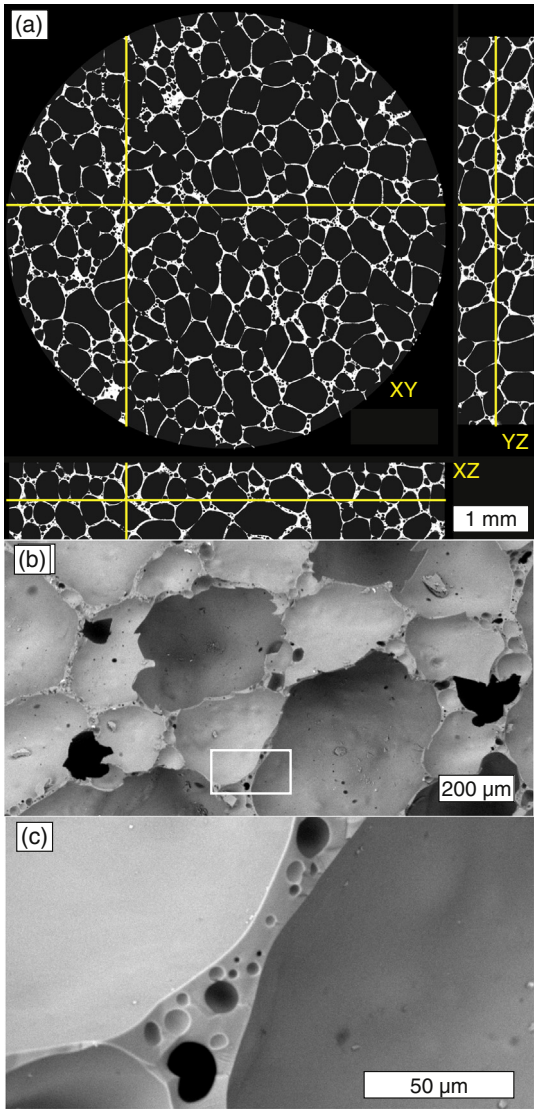

Fig. 1. X-ray computed tomography (XCT) and scanning electron microscopy (SEM) images of FOAMGLAS®. (a) Compiled XCT images of a FOAMGLAS® core (6 × 1 mm) show the distribution of glass (white) and bubbles (dark grey) in three dimensions. The position of the slices shown within the FOAMGLAS® core are indicated by the yellow lines in each orientation (i.e., XY, YZ, XZ). Sub-rounded bubbles 100–275 µm in radius are uniformly distributed within the glass and separated by thin curvilinear glass walls. Smaller bubbles (radii < 25 µm) sit within the glass walls (b, c). Cores do not show bubble wall fracturing as a result of sample preparation. Irregular black shapes in (b) are glass walls cut during sectioning and give view into bubbles. White box in (b) shows location of (c). (For interpretation of the references to colour in this figure legend, the reader is referred to the web version of this article.)

contain gas (> 99.5% CO_2), are sub-rounded, and homogenously distributed within the glass (Fig. 1). The size distribution of the bubbles is bimodal: the volumetrically dominant bubbles have radii between 100 and 275 µm (Fig. 1b), while a second population of smaller bubbles (radii < 25 µm) are present in the glass films that separate bubbles (Fig. 1c).

Table 1 includes the properties of FOAMGLAS® HLB 2400 as reported by Owens Corning [11]. To augment these data we have included the results of our independent characterization and testing of this material using typical methods and analyses in volcanological studies (following sections) (data available in Table 1).

Table 1
Average physical and thermal properties of FOAMGLAS® (HLB 2400) as measured in this study and reported by Owens Corning Corporation (OCC).

Property	Measured	Uncert.	Calculated	Uncert.	OCC
Density (g cm^{-3})[a]					
Dimensional (ρ_{dim})	–	–	0.21	< 0.001	0.20
Skeletal (ρ_{skel})	–	–	0.22	< 0.001	–
Bulk (ρ_{bulk})	–	–	2.41	0.01	–
Porosity[b]					
Total (ϕ_{tot})	–	–	0.91	0.01	–
Connected (ϕ_{con})	–	–	0.06	< 0.01	–
Isolated (ϕ_{iso})	–	–	0.85	0.01	–
Permeability (k; m^2)	< 10^{-18}	–	–	–	0
Thermal conductivity (λ; W m^{-1} K^{-1})					
25–30 °C	0.074	< 0.001	–	–	0.057
150 °C	0.088	0.001	–	–	0.080
Thermal diffusivity (a; m^2 s^{-1})					
25–30 °C	5.38×10^{-7}	0.02×10^{-7}	–	–	–
150 °C	5.19×10^{-7}	0.03×10^{-7}	–	–	–
Specific heat capacity (Cp; J g^{-1} K^{-1})[c]					
25–30 °C	–	–	0.65	0.03	0.77
150 °C	–	–	0.81	0.05	–
VFT fit parameters					
A	−2.14	–	–	–	–
B	4238.96	–	–	–	–
C	498.45	–	–	–	–
Tg (°C) $\eta = 10^{12}$ Pa s	525	–	–	–	–
Melt fragility ("steepness index")	38	–	–	–	–

[a] Calculated from measured mass, and dimensional (caliper) and skeletal (helium pycnometry) volumes (at ambient temperature); uncertainties are propagated from 1σ uncertainty in volume and mass measurements.

[b] $\phi_{tot} = 1 - \rho_{dim}/\rho_{bulk}$; $\phi_{con} = 1 - \rho_{dim}/\rho_{skel}$; $\phi_{iso} = \phi_{tot} - \phi_{con}$; uncertainties in average densities have been propagated to give uncertainties in porosities; connected porosity represents the bubbles that intersect the surface of the prepared cores (see Fig. 1a).

[c] $Cp = \lambda/(\rho_{dim}\ a)$; uncertainties average dimensional density, thermal conductivity and thermal diffusivity have been propagated.

3. Characterization

3.1. Porosity and permeability

Our porosity and permeability measurements are based on cylindrical cores (2.4 × 5.2 cm) prepared (cored and ends ground) from a single sheet of FOAMGLAS® HLB 2400 (45 × 60 × 5.2 cm). Each core was measured at ambient temperature for sample length and diameter using digital calipers, mass using a high precision balance, and skeletal volume (i.e. volume of glass + isolated bubbles) using a Micromeritics AccuPyc II 1340 He-pycnometer. The bulk density of the bubble-free glass was calculated from the mass and volume of chips of re-melted FOAMGLAS® (see Section 3.3) when measured at ambient temperature. From these measurements we determined the average dimensional (ρ_{dim}), skeletal (ρ_{skel}) and bulk (ρ_{bulk}) densities of the glass. The average total (ϕ_{tot}), connected (ϕ_{con}) and isolated (ϕ_{iso}) porosities are calculated from these densities. Table 1 includes these values and relevant equations. Uncertainties in densities and porosities are propagated from the 1σ standard deviation of the measured sample lengths, diameters, masses and skeletal volumes.

The permeability of the FOAMGLAS® cylindrical cores was estimated using the benchtop nitrogen permeameter at the Institut de

Physique du Globe de Strasbourg (IPGS, University of Strasbourg, France) (see Heap et al. [12] and Kushnir et al. [13] for detailed descriptions of the apparatus, methods, and supporting theory). To minimize gas flow along the outer surfaces of the cores, we coated the cylinders with a silicone sealant and placed the coated core within an annular silicone rubber jacket before inserting them into the confining pressure vessel of the apparatus. A confining pressure of 1 MPa was used for all measurements. A transient pulse method was used, with an initial upstream fluid pressure of 2000 mbar and atmospheric conditions as the downstream fluid pressure/reservoir. Test times were restricted to 16 h and conducted overnight to avoid diurnal temperature changes. Over the experimental timescale there was negligible (< 10%) change in the upstream fluid pressure indicating a permeability below the detection limit of the permeameter ($\ll 10^{-18}$ m^2) (Table 1).

In summary, FOAMGLAS® cores have high measured total porosities (~0.91) and remain impermeable following sample preparation processes (Table 1). The gas-accessible porosity (from helium pycnometry; reported in Table 1 as the connected porosity) represents the proportion of bubbles that intersect the surface of the core (e.g. Fig. 1a), rather than bubbles that have been connected as a result of FOAMGLAS® synthesis or coring and grinding.

3.2. Thermal conductivity and diffusivity

The thermal conductivity and diffusivity of the material were measured at ambient temperature (25–30 °C) and 150 °C, using a Hot Disk TPS 500 Thermal Constants Analyzer equipped with a Kapton-insulated sensor (design 5465) at IPGS (see Heap et al. [14] for a detailed description of the apparatus) (Table 1). The sensor was sandwiched between two FOAMGLAS® cores and six consecutive measurements were conducted at five-minute intervals to ensure thermal equilibration of the sample between measurements. The output power was 10 mW, and was applied for 20 s. For measurements at 150 °C, the entire sample assembly was heated within a box furnace (SalvisLab VC20 vacuum oven) and left for 1 h to ensure thermal equilibration. The sample was then placed in the assembly at 150 °C and left for an additional hour prior to the first measurement, again to ensure thermal equilibration. In all thermal analyses, diffusivity and conductivity were measured simultaneously, and the specific heat capacity was calculated by the Hot Disk system from these measurements and the input dimensional density of the glass (0.21 g cm^{-3}). Table 1 includes relevant equations and the uncertainty in these measurements.

At elevated temperatures, the measured thermal conductivity increases, whereas the measured thermal diffusivity decreases (Table 1). The calculated specific heat capacity is also greater at 150 °C than at ambient conditions (Table 1). The measured conductivities and calculated specific heat capacities are, respectively, 9–20% greater and 18% less than values reported by Owens Corning (Table 1). The small size of the Hot Disk sensor (6.2 mm in diameter), and the relatively small contact area between the sensor and the uneven surface of the porous glass (e.g., Fig. 1a) may contribute to the discrepancy between the reported and measured thermal conductivities.

3.3. Viscosity

FOAMGLAS® was prepared for viscosity and calorimetric (Section 3.4) measurements by re-melting samples to produce bubble-free glass chips. Samples were crushed and powdered in an agate mortar, then melted in large thin walled Pt crucibles. Melting was performed in a Nabertherm® MoSi2 box furnace at 1400 °C in multiple, small batches. The crucible was left in the furnace for 1 h to allow for potential melt degassing, and samples were quenched to glass on a steel plate to accelerate cooling and to suppress crystal growth.

Some of the bubble-free FOAMGLAS® glass was re-melted into $Pt_{80}Rh_{20}$ cylindrical crucibles (51 mm height, and 26.6 mm diameter) and transferred into a Deltech® box furnace for high-temperature

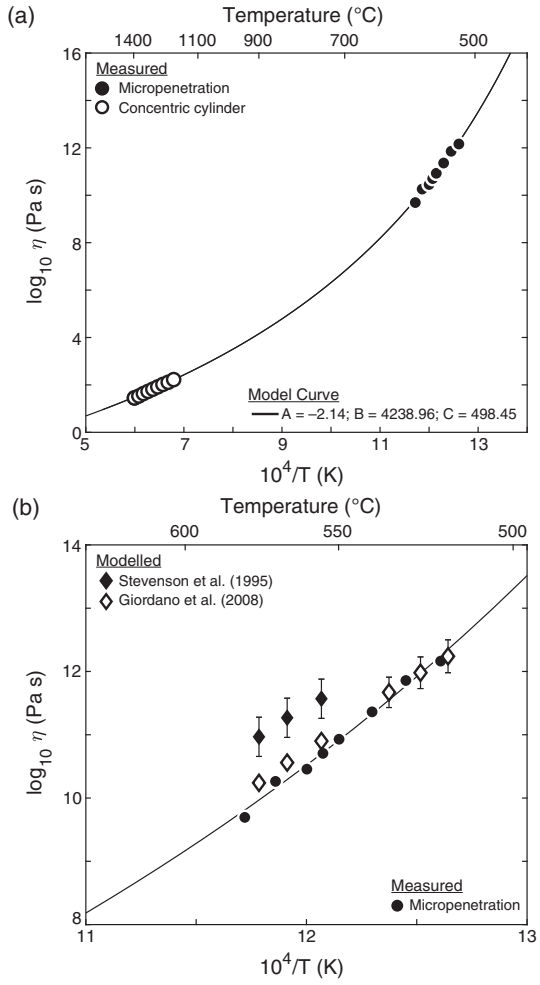

Fig. 2. Viscosity ($\log_{10}\eta$) of FOAMGLAS® melts plotted against temperature (10^4/T (K); °C). Measurement and propagated uncertainties are less than symbol size unless shown otherwise. (a) Melt viscosities measured by micropenetration (closed circles) and concentric cylinder (open circles) viscometry. The curve is the VFT model fitted to the experimental data. (b) Model melt viscosities derived from differential scanning calorimetric data (Fig. 3), based on models of Stevenson et al. [25] (closed diamonds) and Giordano et al. [26] (open diamonds). Solid line is the VFT model curve from (a), which captures the low-temperature viscosity data measured over the same temperature range (closed circles, as in (a)).

rheological experiments. High-temperature viscosity measurements were performed using a Brookfield DV-III + viscometer head (full range of torque = 0–0.7187 mNm). A solid $Pt_{80}Rh_{20}$ spindle is hung from this measurement head, immersed into the sample and rotated at a constant rate. The torque required to maintain a constant rotation rate is proportional to the melt viscosity and is recorded at a frequency of 1 Hz. The spindle used in these experiments is 33.2 mm long with a 45° conical top and bottom (14.4 mm diameter). This bob is hung on a 2.4 mm diameter stem (see details in Dingwell and Virgo [15]). The torque reading for the spindle and crucible were calibrated against the DGG1 standard glass of the Physikalisch-Technische Bundesanstalt (PTB), for which the viscosity-temperature relationship is accurately known. Calibration was performed for shear rates and temperatures exceeding those used in this study. The precision of the viscosity determination is ± 3% as described in Dingwell [16]. The thermal evolution of the sample at the imposed cooling rates was calibrated over the entire experimental temperature range using a platinum sheathed type-S thermocouple immersed in DGG-1 standard glass.

Using this method, we measured melt viscosity at temperatures

from 1370 to 1199 °C, in temperature steps of ~25 °C (Fig. 2a; Table A1). Each temperature step was maintained for 120 min and a stable torque reading was commonly achieved after ~70 min. Torque values measured when returning to a previous high experimental temperature (1395 °C) after measurements at other temperatures stabilized with a reproducibility of ~1% of the measured value. This indicates thermal and chemical (i.e. redox) homogeneity and stability of the sample at the measurement conditions.

Raman spectral analysis of re-melted bubble-free FOAMGLAS® (Fig. B1), both, prior to and after high-temperature viscometry, show: (1) an absence of Raman peaks related to crystalline phases, and (2) no change in the Raman spectra before and after experimentation. These results indicate that the high temperatures imposed during viscometry, calorimetry, and deformation experiments do not cause crystallization or modification of the melt structure. Therefore, all retrieved viscosity or calorimetric data are representative of the FOAMGLAS® HLB 2400 material.

Low-temperature viscosity measurements were carried out on double-polished 3 mm thick samples of the re-melted bubble-free glass using the micropenetration technique [17]. Measurements were conducted between 520 and 580 °C, using a Setaram Setsys vertical dilatometer at the EVPLab of Roma Tre University, Italy [18]. The samples were heated to the target temperature at an initial rate of 25 °C min^{-1}, which was decreased to 10 °C min^{-1} for the last 100 °C to avoid overshooting the target temperature. At the target temperature, the samples were allowed to thermally relax for 10 min, and then a load of 100 g was applied on their surface via a pushing rod with an iridium hemispherical indenter (1 mm radius). Indentation of the hemisphere into the sample was measured as a function of time using a linear variable displacement transducer (LVDT). The rate at which the indenter moved into the melt was used to determine sample viscosity [17]. The system was also calibrated with the standard glass DGG1. At the investigated temperatures, FOAMGLAS® viscosity ranges from $10^{9.7}$ to $10^{12.2}$ Pa s (uncertainty in viscosity measurements is ± 0.06 Pa s $\log_{10}$ units) (Fig. 2a; Table A1).

We have fit the Vogel-Fulcher-Tammann (VFT) equation (i.e. $\log_{10}\eta = A + B/(T - C)$), to the high- and low-temperature viscosity measurements (Fig. 2a; Table A1) to model the temperature-dependence of the melt viscosity [19]. The unweighted fit yields the adjustable parameters A, B and C, as reported in Table 1. Fig. 2a compares the model curve to the data. The model captures all measured viscosities and exactly reproduces the data.

Based on the VFT model fit, the glass transition temperature (Tg), taken as the temperature where melt viscosity is ~10^{12} Pa s, is calculated to be 525 °C (Table 1). Similarly we used the VFT model fit to assess FOAMGLAS® melt fragility: fragility is a parameter that describes the sensitivity of the melt structure to changes in temperature [20,21]. It can be assessed qualitatively by looking at the shape of the VFT model in $\log_{10}\eta - 1/T$ (K) space (e.g., Fig. 2a): strong liquids will have near-Arrhenian temperature dependence while fragile liquids will be non-Arrhenian [20]. A measure of melt fragility is provided by the "steepness index" (m) calculated from the VFT function ($B/(Tg(1 - C/Tg)^2)$). The FOAMGLAS® melt has a non-Arrhenian temperature dependence and a corresponding m of 38 (Table 1).

3.4. Calorimetry

Calorimetric measurements were performed using a Netzsch DSC 404 Pegasus Differential Scanning Calorimeter (DSC) at the EVPLab. The device has been calibrated using melting temperatures of standard materials (inorganic salts of Rb, K, Cs and Ba) up to 1000 °C. For these analyses, a double-polished chip of the re-melted, bubble-free FOAMGLAS® was placed in a Pt/Rh crucible that is continuously flushed with argon (20 L min^{-1}). The sample was heated at 1 °C min^{-1} from ambient temperature to 50 °C, where it was kept for 1 h to achieve DSC signal equilibrium. The sample was then heated at a rate of 20 °C min^{-1} to

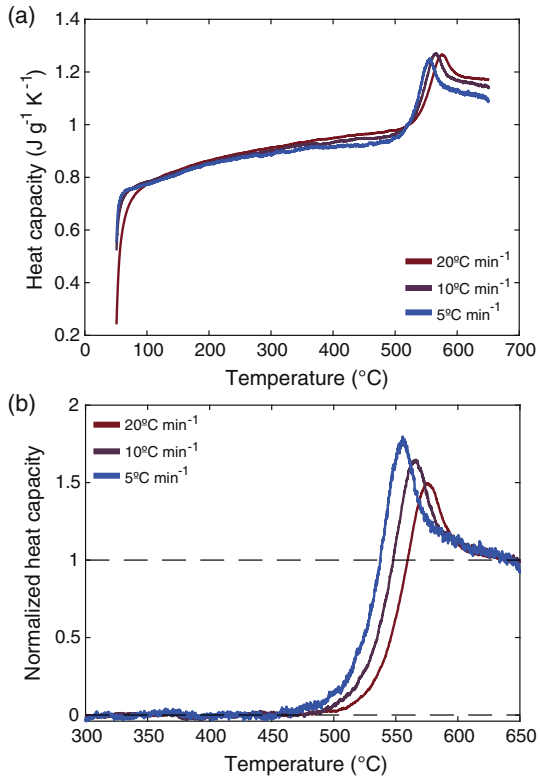

Fig. 3. Differential scanning calorimetry scans of FOAMGLAS® across the glass transition, expressed as (a) absolute and (b) normalized heat capacity curves plotted against temperature (°C). Coloured curves (red, purple, blue) show data collected in subsequent controlled heating-cooling cycles, at decreasing cooling rates. Slower cooling rates cause curves to shift to lower temperatures and peaks of normalized heat capacity to increase. Glass transition temperatures (Tg^{onset}, Tg^{peak}, Tg^{liquid}) were picked from the absolute heat capacity curves after Giordano et al. [26]. (For interpretation of the references to colour in this figure legend, the reader is referred to the web version of this article.)

~50 °C above the estimated Tg of the glass. Measurements of Tg were performed in three subsequent thermal treatments where the heating rates matched the previous cooling rates, which decreased from 20 to 10 to 5 °C min^{-1} (coloured curves, Fig. 3). To convert raw DSC signals to absolute heat capacity values (Cp, J g^{-1} °C^{-1}), a baseline measurement was taken where two empty Pt/Rh crucibles were loaded into the DSC and then the DSC was calibrated against the Cp of a single sapphire crystal [22]. The heat capacity versus temperature paths do not show any evidence of crystallization during the experiments (Fig. 3a), as also confirmed by post run optical analysis (Appendix B).

Table 2 includes the glass transition temperatures (Tg^{onset}, Tg^{peak}, Tg^{liquid}) determined from the absolute heat capacity curves for different prescribed cooling rates (Fig. 3a). As the cooling rates decrease the measured glass transition temperatures also decrease by 8–11 °C. Following the method of Wilding et al. [23], the normalized ($Cp_{glass} = 0$ and $Cp_{liquid} = 1$) heat capacity curves (Fig. 3b) can be directly

Table 2
Differential scanning calorimetry measured glass transition temperatures (Tg) at different cooling rates (|q|), fictive temperatures (T_f), activation energy for the relaxation of enthalpy (ΔH*), and the pre-exponential term (A) (see text).

|q| (°C min^{-1})	Tg^{liquid} (°C)	Tg^{peak} (°C)	Tg^{onset} (°C)	T_f (°C)
20	651	575	535	528
10	640	566	526	510
5	628	556	518	494
ΔH* (kJ mol^{-1})	430.41	406.07	430.18	–
$\log_{10}$ A (K s^{-1})	−23.85	−24.50	−27.33	–

correlated to the evolution of the fictive temperature (T_f), which defines the structure of the glass (Table 2). The modelled T_f values decrease by 16–18 °C as the cooling rate decreases.

In order to model and predict FOAMGLAS® heat capacity evolution and the glass transition temperature as a function of cooling rate, we used our DSC data to determine the activation energy for enthalpic relaxation of the glass (ΔH^*, kJ mol^{-1}), following the methods in the relaxation geospeedometry literature [24,23]. This parameter can be calculated from the measured glass transitions temperatures (Tg^x, °C) at the different cooling/heating rates ($|q|$, °C s^{-1}) using the following equation: $-\ln|q| = -\ln A + \Delta H^*/(R\ Tg^x)$, where A is the pre-exponential term and R is the universal gas constant (Table 2).

Lastly, we have used the DSC results and the models of Stevenson et al. [25] and Giordano et al. [26] to calculate the implied melt viscosity at the glass transition for different cooling rates. These models apply a shift factor to the calorimetric measurements in order to predict the effective viscosity of the melt as the glass transition is reached [25]. The Giordano et al. [26] model results (open diamonds, Fig. 2b) agree well with the VFT model curve fitted to the measured viscosities in the same temperature range. The Stevenson et al. [25] model results are nearly an order of magnitude greater than model curves (closed diamonds, Fig. 2b).

4. A case study using FOAMGLAS®: the rheology of bubbly melts

Studies of the rheology of vesicular magmas commonly document decreasing bulk viscosity with increasing porosity (see Mader et al. [5] and Vona et al. [6] for compilations of models and experimental data). However the relationship of porosity to bulk viscosity is complex and depends on bubble size, shape, orientation and deformation rate (Mader et al. [5] and references therein). Studies of the deformation of other cellular solids [27–30] suggest magma viscosity will also depend on the capacity of gases within void spaces to become pressurized during deformation, which is a function of their connectivity. “Closed-cell” foams contain bubbles that are isolated from one another and from the atmosphere. Examples of closed-cell magmas may include magmas in the conduit prior to fragmentation, pyroclasts or lavas that vesiculate en route to or at the surface, and extensively welded granular materials (i.e. where inter-particle spaces have become isolated [31]). Materials science studies of closed-cell foams show when these impermeable foams are loaded, gases trapped within bubbles are compressed, and gas overpressures develop in individual bubbles [27,28]. The pressurized gas resists further deformation and exerts a restorative pressure on the surrounding cell walls [27,28]. In contrast, “open-cell” foams contain void spaces that are interconnected and communicate with the atmosphere. Examples of open-cell magmas may include magmas following fragmentation, welding pyroclastic materials, and lavas with interconnected pores. When loaded, the gas within the void spaces can move through or out of the permeable material. The gas therefore has no capacity to become pressurized [27,28]. Because it exclusively contains isolated bubbles, as shown by the measured isolated porosity and estimated permeability (Table 1), FOAMGLAS® is an excellent experimental proxy for the former materials and is not a suitable material to use when studying the rheology of open-cell foams.

There have been few studies that have sought to distinguish the bulk viscosities and rheological behaviours of closed- vs. open-cell magmatic foams [32]. Below we compare the results of our deformation experiments using closed-cell FOAMGLAS® (Section 4.1) to high-temperature uniaxial deformation experiments that used open-cell volcanic materials with high connected porosities (e.g., cores of sintered particles [8,33–37], vesicular lavas [38–41], vesicular glasses [3,6]). From this comparison we identify the different rheologies of closed- vs. open-cell magmas: the ways strain accumulates in these materials are distinct, as are the causes of observed strain-hardening behaviour.

4.1. Deformation experiments

We performed unconfined, uniaxial compression experiments to explore the behaviour of FOAMGLAS® deforming at temperatures above *Tg*. The high-temperature experiments use the low-load, Volcanic Deformation Rig (VDR) at the University of British Columbia, Canada [42]. The sample assembly includes a tube furnace; the temperature of the furnace is controlled by one K-type thermocouple and simultaneously measured by two additional K-type thermocouples. Samples were heated at 5 °C min^{-1} to the experimental temperature (555 °C). The measured melt viscosity at this temperature is $10^{10.7}$ Pa s (Fig. 2; Table A1). The samples remained at the experimental temperature for 45 min prior to deformation to ensure the melt was relaxed and thermally homogenous. Cores were then shortened at a constant strain rate of 2.5×10^{-5} s^{-1} to different final positions equivalent to 0.005–0.60 strain (ε_i). Throughout deformation an LVDT positioned beneath the moving platen measured sample shortening (displacement), and a 2.5 klb load cell at the top of the sample assembly measured the load on the sample. In most experiments, the displacement direction was reversed following deformation and the sample was unloaded over a period of 5 min, then cooled at 5 °C min^{-1}. In two confined experiments the samples were not unloaded but cooled at 5 °C min^{-1} while in contact with the upper piston. Following cooling, sample dimensions and porosity were remeasured (Table 3).

The behaviour of FOAMGLAS® above *Tg* is consistent: nine stress-strain curves from samples deformed to different amounts of total strain (ε_i = 0.01–0.60) plot on top of each other (Fig. 4a). This consistency is a function of the textural homogeneity of the FOAMGLAS® material, and its capacity to be shaped, handled and prepared for experiments without measurable changes to its physical properties. The variation (~0.01 MPa) in the position of the plateau in the curves can be attributed to slightly different experimental temperatures (555 ± 2 °C).

The mechanical data show FOAMGLAS® cores behave viscously: there are no sudden drops in the stress-strain curves with increasing strain – no fracturing events were recorded (Fig. 4a). The stress-strain curves show three stages of deformation (Fig. 4a): where strain is low ($\varepsilon_i < 0.005$) stress increases sharply with increasing strain, as the bubble-rich melt is initially loaded. As deformation continues ($0.005 < \varepsilon_i < 0.15$) the measured stress on the sample plateaus near ~0.05 MPa. This behaviour continues until strain is > 0.15, where stress increases with increasing strain, indicating strain-hardening behaviour. The potential causes of this strain-hardening behaviour are discussed further in Section 4.3.

Photographs (Fig. 4b) and scanning electron microscopy (SEM) images (Fig. 4c) of the experimental products confirm the FOAMGLAS® cores did not fracture (microscopically or macroscopically) during deformation. With increasing applied strain cores shorten and their diameters increase (Fig. 4b). Measured changes in sample dimensions show significant volume loss, up to 9.3 cm^3, or 38% of the original volume, also occurred as a result of deformation (Table 3).

The total porosities of the cores decrease from 0.91 to 0.85 with increasing applied strain. The small magnitude of the change in total porosity (0.06) relative to the change in the volume (up to 38%) is a consequence of the high gas:solid ratio of FOAMGLAS®. On average an undeformed core has a dimensional volume of 23.84 cm^3, dimensional density of 0.21 g cm^{-3} and total porosity of 0.91 (Table 1). Therefore, on average, 21.69 cm^3 of a core is occupied by gas and 2.15 cm^3 by glass. While a 30% reduction in volume (for example) changes the volume occupied by gas to 15.18 cm^3, and increases the dimensional density to 0.28 g cm^{-3} (a 30% increase), the normalization of this final dimensional density to the high bulk density of the glass (2.41 g cm^{-3}) yields a final total porosity of 0.88, a reduction of just 0.03. Lastly, measured isolated porosities remain high (> 0.79; Table 3) following deformation. This demonstrates deformation did not result in an increase in bubble connectivity.

Table 3
Physical properties of experimental products, including the instrumental strain (ε_i), the changes in sample length (l), radius (r) and dimensional volume (V), total and isolated porosity (ϕ) after deformation, and shortening (ε_s), radial (ε_r) and axial (ε_a) strains.

Sample	ε_i	Δl (cm)	1σ	Δd (cm)	1σ	ΔV_{dim} (cm^3)	Uncert.	ϕ				ε_s[a]	Uncert.	ε_r[a]	Uncert.	ε_a[a]	Uncert.
								Total	Uncert.	Isolated	Uncert.						
fg_19	0.005	−0.04	0.00	0.00	0.01	−0.12	0.06	0.92	0.01	0.85	0.01	0.009	0.001	0.003	0.000	0.006	0.003
fg_20	0.005	−0.05	0.00	0.01	0.01	−0.08	0.05	0.92	0.01	0.85	0.01	0.010	0.001	0.006	0.000	0.004	0.004
fg_18	0.01	−0.07	0.00	0.00	0.01	−0.22	0.07	0.91	0.01	0.85	0.01	0.014	0.001	0.004	0.000	0.010	0.005
fg_22	0.01	−0.08	0.00	0.01	0.00	−0.16	0.05	0.92	0.00	0.85	0.00	0.015	0.001	0.008	0.000	0.007	0.003
fg_16	0.015	−0.10	0.00	0.01	0.01	−0.33	0.07	0.92	0.01	0.85	0.01	0.020	0.000	0.005	0.000	0.015	0.004
fg_17	0.015	−0.10	0.00	0.01	0.01	−0.24	0.09	0.91	0.01	0.85	0.01	0.020	0.001	0.009	0.000	0.011	0.006
fg_15	0.02	−0.13	0.00	0.01	0.01	−0.42	0.08	0.91	0.01	0.85	0.01	0.025	0.000	0.006	0.000	0.020	0.005
fg_21	0.02	−0.13	0.00	0.01	0.01	−0.29	0.11	0.91	0.01	0.84	0.01	0.025	0.001	0.012	0.000	0.013	0.006
fg_109	0.05	−0.30	0.01	0.03	0.02	−0.87	0.20	0.90	0.01	0.84	0.01	0.057	0.001	0.023	0.000	0.035	0.008
fg_122	0.05	−0.29	0.00	0.02	0.01	−0.82	0.10	0.91	0.01	0.84	0.01	0.055	0.000	0.020	0.000	0.035	0.004
fg_110	0.10	−0.53	0.00	0.06	0.03	−1.53	0.26	0.91	0.01	0.84	0.01	0.102	0.001	0.044	0.000	0.061	0.010
fg_116	0.10	−0.52	0.00	0.04	0.03	−1.77	0.23	0.91	0.01	0.84	0.01	0.100	0.001	0.032	0.000	0.070	0.010
fg_108	0.20	−0.98	0.00	0.11	0.07	−2.85	0.58	0.90	0.02	0.83	0.02	0.187	0.001	0.082	0.002	0.114	0.023
fg_121	0.20	−1.01	0.00	0.08	0.05	−3.49	0.47	0.90	0.02	0.85	0.02	0.194	0.001	0.065	0.001	0.138	0.019
fg_106	0.30	−1.45	0.00	0.16	0.08	−4.65	0.61	0.89	0.03	0.84	0.03	0.276	0.001	0.114	0.003	0.183	0.024
fg_117	0.30	−1.42	0.00	0.15	0.06	−4.26	0.49	0.90	0.02	0.82	0.02	0.274	0.001	0.113	0.003	0.181	0.021
fg_104	0.40	−1.92	0.00	0.18	0.12	−6.86	0.83	0.88	0.04	0.84	0.04	0.368	0.001	0.133	0.006	0.271	0.033
fg_118	0.40	−1.79	0.01	0.20	0.13	−5.83	0.92	0.88	0.04	0.85	0.04	0.342	0.001	0.143	0.007	0.233	0.037
fg_115	0.50	−2.28	0.00	0.27	0.14	−7.39	0.85	0.88	0.04	0.83	0.04	0.438	0.001	0.189	0.010	0.307	0.035
fg_120	0.50	−2.30	0.00	0.34	0.19	−6.79	1.21	0.88	0.06	0.82	0.06	0.438	0.001	0.229	0.015	0.271	0.048
fg_112	0.60	−2.61	0.01	0.42	0.17	−7.80	1.04	0.87	0.05	0.79	0.05	0.498	0.001	0.270	0.016	0.312	0.042
fg_119	0.60	−2.55	0.01	0.38	0.16	−7.54	0.95	0.88	0.05	0.82	0.05	0.493	0.001	0.255	0.015	0.319	0.040
fg_123[b]	0.20	−1.05	0.00	0.13	0.06	−2.74	0.52	0.90	0.02	–	–	0.202	0.001	0.097	0.002	0.116	0.022
fg_124[b]	0.60	−3.09	0.00	0.56	0.25	−9.34	1.28	0.85	0.07	–	–	0.592	0.000	0.340	0.029	0.382	0.052

Note: Uncertainties in volume, porosity and strain have been propagated from the 1σ standard deviation in sample length, diameter and mass, and the bulk density (Table 1).

[a] After Quane and Russell [34].

[b] Confined samples (Section 4.1); samples were cut for thin sections without measuring skeletal volume, so isolated porosities are unknown.

4.2. Strain analysis

Following the work and nomenclature of Quane and Russell [34], we used the measured changes in sample length, radius, and volume to calculate shortening strain (ε_s), radial strain (ε_r) and axial (i.e. volumetric) strain (ε_a), respectively (Table 3). We propagated measurement uncertainties for sample length, diameter and dimensional volume to determine the uncertainties in calculated strain parameters (Table 3). In Fig. 5 we use the descriptive terms “bulging” and “volume loss” to represent radial and axial strains, respectively, and have plotted these parameters against instrumental strain (ε_i). Fig. 5a shows that many cores deformed to > 0.30 strain record less shortening than the applied displacement (open circles fall below the 1:1 line). In experiments where cores where not unloaded after deformation (confined samples), the sample shortening equals the instrumental strain (closed symbols, Fig. 5a). The discrepancy between the shortening and instrumental strains in many of the samples above 0.30 strain is a consequence of unloading the deformed closed-cell foam: prior to cooling below *Tg* (it takes ~7.5 min to cool below Tg^{onset} at a rate of 5 °C min^{-1}) the isolated pressurized bubbles expanded in the absence of an external load in order to lower their internal gas pressure. As a result, the gas in the bubbles caused the core to viscously “rebound” and sample length to increase. This response does not occur during the compression of open-cell materials because the gases present have no capacity to become pressurized. This potential for high-porosity closed-cell foams to resist deformation and rebound highlights an important difference in the responses of closed- and open-cell magmatic foams to deformation.

FOAMGLAS® deforms by a combination of bulging and volume loss (Fig. 5b), though volume loss is the dominant mechanism for accommodating the resultant strains (Fig. 5c). In contrast, in many experimental studies of open-cell vesicular melts and magmas, the bulging component is greater than the volume loss component until total strain is ~0.40 [6,34,35,39]. Again, the change in deformation behaviour can likely be attributed to the presence, and abundance, of isolated bubbles in the FOAMGLAS®.

4.3. Causes of strain-hardening

In addition to generating a gas overpressure within the individual cells, studies of the mechanical behaviour of closed-cell foams (e.g., polymers, ceramics, metals) have shown compression will cause cell walls to reorient, and to stretch or buckle depending on their orientation to the principle stress [27,28,30]. As a consequence of these two mechanisms, the stiffness of two-phase closed-cell materials will increase throughout deformation, and strain-hardening behaviour will be apparent in the mechanical data [27,28].

FOAMGLAS® cores show the expected strain-hardening behaviour, which becomes more pronounced above 0.15 strain (Fig. 4a). In these cores bubble walls are deformed: walls oriented normal to the shortening direction have been stretched and flattened, and bubble walls oriented parallel to the shortening direction have been bent and buckled (Fig. 4c). Notably, though extensively deformed, bubble walls are intact. Coupled with the high measured isolated porosities of the experimental products (> 0.79, Table 3), and the rebound behaviour observed (Section 4.2), we submit that gas loss did not occur as a result of deformation.

Two additional material properties may affect the observed strain-hardening behaviour. First, as strain increases, the initially high gas:-solid ratio decreases when bubbles are compressed. An increase in this ratio, which is poorly captured by the measured change in total porosity (Section 4.1), will result in a stiffer composite, and greater forces required to deform the material (e.g. Fig. 4a). In addition FOAMGLAS® cores bulge to accommodate strain (Fig. 4b). Therefore the contact areas (i.e. diameters of end-faces) increase slightly with increasing strain (e.g. high strain sample in Fig. 4b). However, the reduction in the maximum calculated stress as a function of the change in contact area is small (~0.025 MPa for high strain sample), and is much less than the stress increase as a result strain-hardening (~0.1 MPa) (Fig. 4a).

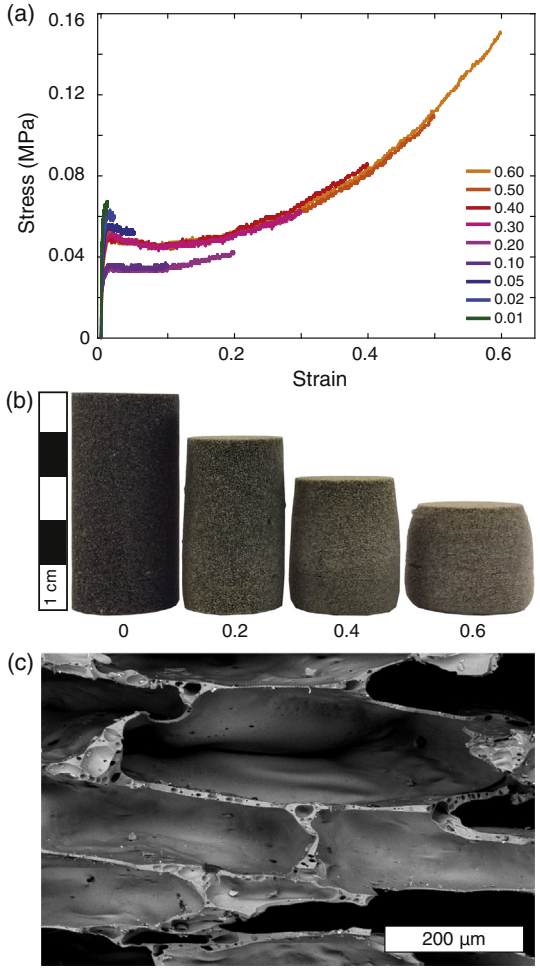

Fig. 4. Results of high-temperature uniaxial compression experiments. (a) Stress–strain curves, colour-coded for applied instrumental strain. Isothermal experiments show the cores to deform viscously at temperatures (555 ± 1–2 °C) above *Tg* and exhibit strain-hardening behaviour above 0.15 strain. Stress calculated using initial sample area. (b) Photos of an undeformed FOAMGLAS® core (left) and cores shortened by 0.20, 0.40 and 0.60 instrumental strain. With increasing strain, cores show more pronounced bulging but no macroscopic fractures develop. Units of scale bar at left are 1 cm. (c) SEM image of deformed bubbles in a core shortened by 0.60 instrumental strain (image in same orientation as cores shown in (b)). As a result of shortening large bubbles have become nearly rectangular. Bubble walls are intact.

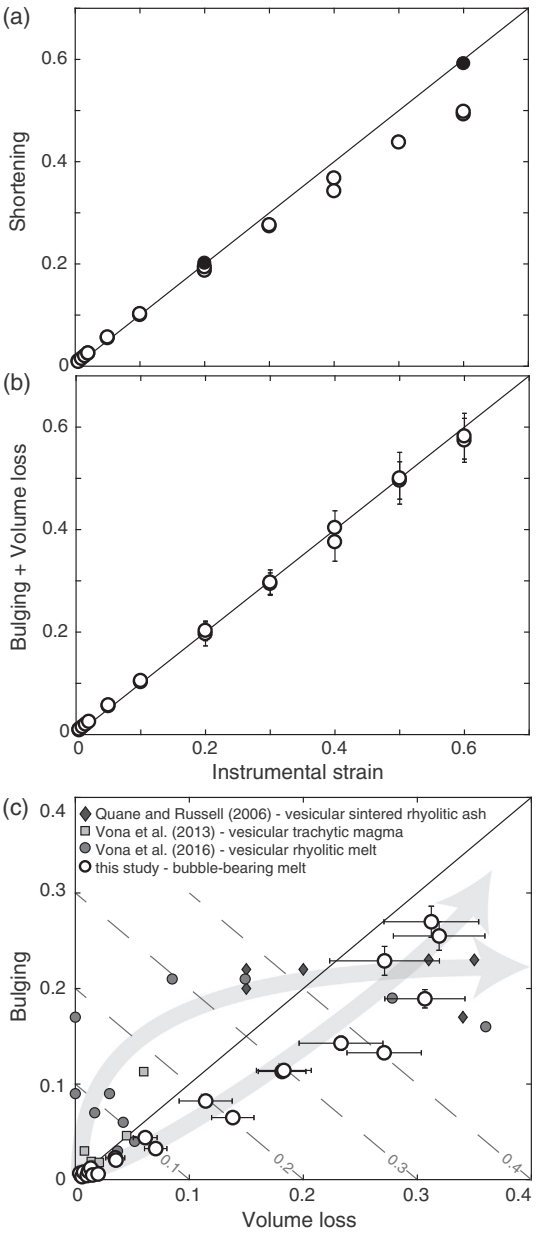

Fig. 5. Strain analysis. Solid line shows 1:1 relationship between parameters. Measurement and propagated uncertainties (Table 3) are less than symbol size unless shown otherwise. (a) Sample shortening against instrumental strain. Open circles show samples that were unloaded following deformation. The sample lengths measured after cooling are less than the applied strain when the instrumental strain was > 0.30. In contrast, closed circles show "confined" samples that were cooled below *Tg* in contact with the upper piston. (b) Combined sample bulging (i.e. radial strain) and volume loss (i.e. axial strain) vs. applied instrumental strain. (c) Comparison of bulging to volume loss. Dashed lines are iso-strain contours, showing total strain. FOAMGLAS® cores (open circles) lie below the 1:1 line (within uncertainty), indicating the closed-cell cores primarily accommodate strain by volume loss. In contrast, open-cell volcanic melts/magmas (filled symbols, above 1:1 line) accommodate strain by bulging below 0.40 total strain, then show increased contribution of volume loss in taking up applied strains > 0.40.

This strain-hardening behaviour can be compared to that of open-cell foams where there is no pressurized gas to support bubble walls and act against the applied stress. In these materials interconnected void spaces will collapse during compression [27,28]. As cells collapse, cell walls touch and interact, and deformation is solely accommodated by the melt [27,28]. This produces strain-hardening behaviour, although the mechanisms giving rise to strain-hardening differ [27–29]. In the volcanology literature, high-temperature deformation of open-cell volcanic materials (i.e., lavas, glasses and granular materials with high connected porosities) causes pore collapse and produces dense composites [6,8,33–41]. As an example, photomicrographs of sintered ash cores (initial porosity ~0.70) track the collapse of inter-grain pore spaces in progressively more dense experimental products (minimum final porosity ~0.25) [8]. As pores collapse and the total porosity decreases, the bulk viscosity of the material increases and produces the observed strain-hardening behaviour [8,34,35].

In conclusion, the results from these high-temperature uniaxial experiments, which use FOAMGLAS® as the experimental material, indicate: (1) the partitioning of strain between bulging and volume loss is dependent on the gases trapped in the isolated void spaces, (2) the mechanisms giving rise to strain-hardening behaviour in vesicular melts are fundamentally different in closed- and open-cell foams, and (3) because isolated bubbles do not collapse under an applied load as connected pores do, melts containing high proportions of isolated bubbles retain their high porosities even after extensive compression

and, moreover, have the potential to rebound and fill available space when the load acting on them is removed.

4.4. Implications for volcanic systems

These results demonstrate that when high-porosity, low-permeability (closed-cell) foams are deformed isolated gas-filled bubbles are compressed and become pressurized, rather than collapsing and expelling their gas. This behaviour has two important consequences for volcanic activity: (1) deforming magmas/lavas can maintain high porosities, and thus low bulk viscosities, as they flow, and (2) throughout deformation magmas/lavas can retain, and also transmit, pressurized gases, that have the potential to cause viscous rebound (as in our experiments) or magmatic fragmentation when deformation ceases. These responses of isolated bubbles to deformation will not only impact the behaviour of magmas in the subsurface, but will also influence the morphology of surficial lava flows, and dictate the potential for explosive activity emanating from these lava flows.

5. Conclusions

The presence of bubbles in silicate and other melts changes the bulk properties of the material significantly. Our understanding of and capacity to predict the effects of bubbles on the physical, thermal and rheological properties of bubble-rich melts requires careful and insightful experimentation. The experimental campaigns must also be carried out at relevant experimental conditions, including at temperatures above *Tg*, during both compaction and simple shear conditions, and in the presence of a pore fluid or other confining pressure. Use of an experimental material like FOAMGLAS® provides a strong basis for relevant experimentation because it is a homogeneous, bubble-rich glass which has constant physical properties, is not susceptible to crystal formation or compositional changes at high temperatures, and has robust, reproducible mechanical behaviour. In this regard it is an excellent proxy for industrial and geological foams and is suitable for use at a wide range of experimental conditions. Given its experimental consistency and reproducibility, FOAMGLAS® can also be used to determine the time (or strain) dependent evolution of the physical properties and rheology of glass or melt foams. With this in mind we recommend that a closed-cell solid like FOAMGLAS® be used in future comprehensive studies of the behaviour of melts, glasses and other cellular materials populated with isolated bubbles, with application to complex natural systems.

Author contribution

A. Ryan designed and carried out the deformation experiments, measured sample properties, and prepared the manuscript with contributions from all co-authors. S. Kolzenburg prepared materials for viscometry, calorimetry and Raman spectroscopy, and completed the concentric cylinder viscosity measurements. A. Vona was responsible for Raman spectroscopy, calorimetry, micropenetration viscometry, and geospeedometry modelling. M. Heap measured sample permeability (with A. Ryan). J.K. Russell fit the VFT model. S. Badger provided the experimental material.

Competing interests

Author S. Badger is employed by Owens Corning Corporation, the maker of FOAMGLAS®. The other authors declare that they have no conflict of interest.

Acknowledgements

This study was supported by the Natural Sciences and Engineering Research Council of Canada (NSERC) Discovery Grants program (J.K. Russell). S. Kolzenburg acknowledges financial support from a H2020 Marie Skłodowska-Curie Actions fellowship DYNAVOLC – No.795044. J.I. Farquharson and A.R.L. Kushnir are thanked for their role in the development and maintenance of the permeameter at IPG Strasbourg. A.R.L. Kushnir is thanked for her help using the Hot Disk Thermal Constants Analyzer. O. Lengliné, and P. Baud are thanked for their role in the acquisition of the Hot Disk Thermal Constants Analyzer. D. B. Dingwell at the Department für Geo- und Umweltwissenschaften, Ludwig-Maximilians-Universität München is thanked for laboratory support for high temperature viscometry. We thank three anonymous reviewers for their constructive comments that helped to improve this manuscript.

Appendix A. Supplementary data

This work is accompanied by two appendices (A, B), containing supplementary information, figures and tables. Supplementary data to this article can be found online at https://doi.org/10.1016/j.nocx.2018.100001.

References

[1] H.M. Gonnermann, M. Manga, The fluid mechanics inside a volcano, Annu. Rev. Fluid Mech. 39 (2007) 321–356.
[2] N.S. Bagdassarov, D.B. Dingwell, Thermal properties of vesicular rhyolite, J. Volcanol. Geoth. Res. 60 (1994) 179–191.
[3] N.S. Bagdassarov, D.B. Dingwell, A rheological investigation of vesicular rhyolite, J. Volcanol. Geoth. Res. 50 (1992) 307–322.
[4] E.W. Llewellin, H.M. Mader, S.D.R. Wilson, The rheology of a bubbly liquid, Proc. R. Soc. Lond. A 458 (2002) 987–1016.
[5] H.M. Mader, E.W. Llewellin, S.P. Mueller, The rheology of two-phase magmas: a review and analysis, J. Volcanol. Geoth. Res. 257 (2013) 135–158.
[6] A. Vona, A.G. Ryan, J.K. Russell, C. Romano, Models for viscosity and shear localization in bubble-rich magmas, Earth Planet. Sci. Lett. 449 (2016) 26–38.
[7] Y. Zhang, A criterion for the fragmentation of bubbly magma based on brittle failure theory, Nature 402 (1999) 648.
[8] S.L. Quane, J.K. Russell, E.A. Friedlander, Time scales of compaction in volcanic systems, Geology 37 (2009) 471–474.
[9] FOAMGLAS®, https://industry.foamglas.com/en-gb/home , Accessed date: 15 November 2018.
[10] FOAMGLAS® Datasheets, https://industry.foamglas.com/en-gb/resources/datasheets , Accessed date: 15 November 2018.
[11] FOAMGLAS® HLB 2400 Product Data Sheet, https://industry.foamglas.com/-/media/industry/files/en/products/pds-us/pds-us/fg-hlb-2400-pdsusa110117.pdf/ , Accessed date: 15 November 2018.
[12] M.J. Heap, A.R.L. Kushnir, H.A. Gilg, F.B. Wadsworth, T. Reuschlé, P. Baud, Microstructural and petrophysical properties of the Permo-Triassic sandstones (Buntsandstein) from the Soultz-sous-Forêts geothermal site (France), Geotherm. Energy 5 (2017) 26.
[13] A.R.L. Kushnir, M.J. Heap, P. Baud, Assessing the role of fracture on the permeability of the Permo-Triassic sandstones at Soultz-sous-Forêts (France) geothermal site, Geothermics 74 (2018) 181–189.
[14] M. Heap, A. Kushnir, L. Griffiths, F. Wadsworth, G.M. Marmoni, M. Fiorucci, S. Martino, P. Baud, H.A. Gilg, T. Reuschlé, Fire resistance of the Mt. Epomeo Green Tuff, a widely-used building stone on Ischia Island (Italy), Volcanica 1 (2018) 33–48.
[15] D.B. Dingwell, D. Virgo, Viscosities of melts in the Na_2O-FeO-Fe_2O_3-SiO_2 system and factors controlling relative viscosities of fully polymerized silicate melts, Geochim. Cosmochim. Acta 52 (1988) 395–403.
[16] D.B. Dingwell, Viscosity-temperature relationships in the system $Na_2Si_2O_5$-$Na_4Al_2O_5$, Geochim. Cosmochim. Acta 50 (1986) 1261–1265.
[17] K.-U. Hess, D.B. Dingwell, S.L. Webb, The influence of excess alkalis on the viscosity of a haplogranitic melt, Am. Mineral. 80 (1995) 297–304.
[18] D. Di Genova, C. Romano, M. Alletti, V. Misiti, P. Scarlato, The effect of CO_2 and H_2O on Etna and Fondo Riccio (Phlegrean Fields) liquid viscosity, glass transition temperature and heat capacity, Chem. Geol. 377 (2014) 72–86.
[19] G.S. Fulcher, Analysis of recent measurements of the viscosity of glasses, J. Am. Ceram. Soc. 8 (1925) 339–355.
[20] C.A. Angell, Relaxation in liquids, polymers and plastic crystals - strong/fragile patterns and problems, J. Non-Cryst. Solids 131 (1991) 13–31.
[21] D.J. Plazek, K.L. Ngai, Correlation of polymer segmental chain dynamics with temperature-dependent time-scale shifts, Macromolecules 24 (1991) 1222–1224.
[22] R.A. Robie, B.S. Hemingway, J.R. Fisher, Thermodynamic Properties of Minerals and Related Substances at 298.5 K and 1 bar (105) Pascals and at Higher Temperatures, U.S. Government Printing Office, Washington, DC, 1979.
[23] M.C. Wilding, S.L. Webb, D.B. Dingwell, Evaluation of a relaxation geospeedometer for volcanic glasses, Chem. Geol. 125 (1995) 137–148.
[24] J. Gottsmann, D.B. Dingwell, Cooling dynamics of spatter-fed phonolite obsidian flows on Tenerife, Canary Islands, J. Volcanol. Geoth. Res. 105 (2001) 323–342.

[25] R.J. Stevenson, D.B. Dingwell, S.L. Webb, N.S. Bagdassarov, The equivalence of enthalpy and shear stress relaxation in rhyolitic obsidians and quantification of the liquid-glass transition in volcanic processes, J. Volcanol. Geoth. Res. 68 (1995) 297–306.
[26] D. Giordano, M. Potuzak, C. Romano, D.B. Dingwell, M. Nowak, Viscosity and glass transition temperature of hydrous melts in the system $CaAl_2Si_2O_8$ - $CaMgSi_2O_6$, Chem. Geol. 256 (2008) 203–215.
[27] L.J. Gibson, M.F. Ashby, Cellular Solids: Structure and Properties, ed. 2, Cambridge University Press, Cambridge UK, 1999.
[28] M. Scheffler, P. Colombo, Cellular Ceramics: Structure, Manufacturing, Properties and Applications, WILEY-VCH, Weinheim Germany, 2005.
[29] F. Fischer, G.T. Lim, U.A. Handge, V. Altstadt, Numerical simulation of mechanical properties of cellular materials using computed tomography analysis, J. Cell. Plast. 45 (2009) 441–460.
[30] S. Meille, Lombardi, J. Chevalier, L. Montanaro, Mechanical properties of porous ceramics in compression: on the transition between elastic, brittle and cellular behavior, J. Eur. Ceram. Soc. 32 (2012) 3959–3967.
[31] F.B. Wadsworth, J. Vasseur, E.W. Llewellin, J. Schauroth, K.J. Dobson, B. Scheu, D.B. Dingwell, Sintering of viscous droplets under surface tension, Proc. R. Soc. A. 472 (2016) 20150780.
[32] S. Sicola, A. Vona, C. Romano, A.G. Ryan, J.K. Russell, In-situ high-temperature rheology of pore-bearing magmas, EGU General Assembly, Vienna, Austria, 8–13 April 2018, 2018 (EGU2018-13349).
[33] S.L. Quane, J.K. Russell, Welding: insights from high-temperature analogue experiments, J. Volcanol. Geoth. Res. 142 (2005) 67–87.
[34] S.L. Quane, J.K. Russell, Bulk and particle strain analysis in high-temperature deformation experiments, J. Volcanol. Geoth. Res. 154 (2006) 63–73.
[35] G. Robert, J.K. Russell, D. Giordano, Rheology of porous volcanic materials: high-temperature experimentation under controlled water pressure, Chem. Geol. 256 (2008) 216–230.
[36] J. Vasseur, F.B. Wadsworth, Y. Lavallée, K.U. Hess, D.B. Dingwell, Volcanic sintering: timescales of viscous densification and strength recovery, Geophys. Res. Lett. 40 (2013) 5658–5664.
[37] M.J. Heap, S. Kolzenburg, J.K. Russell, M.E. Campbell, J. Welles, J.I. Farquharson, A. Ryan, Conditions and timescales for welding block-and-ash flow deposits, J. Volcanol. Geoth. Res. 289 (2014) 202–209.
[38] J.E. Kendrick, Y. Lavallée, K.U. Hess, M.J. Heap, H.E. Gaunt, P.G. Meredith, D.B. Dingwell, Tracking the permeable porous network during strain-dependent magmatic flow, J. Volcanol. Geoth. Res. 260 (2013) 117–126.
[39] A. Vona, C. Romano, D. Giordano, J.K. Russell, The multiphase rheology of magmas from Monte Nuovo (Campi Flegrei, Italy), Chem. Geol. 346 (2013) 213–227.
[40] P.A. Ashwell, J.E. Kendrick, Y. Lavallée, B.M. Kennedy, K.-U. Hess, F.W. von Aulock, F.B. Wadsworth, J. Vasseur, D.B. Dingwell, Permeability of compacting porous lavas, J. Geophys. Res. Solid Earth 120 (2015), https://doi.org/10.1002/2014JB011519.
[41] M.J. Heap, M. Violay, F.B. Wadsworth, J. Vasseur, From rock to magma and back again: the evolution of temperature and deformation mechanism in conduit margin zones, Earth Planet. Sci. Lett. 463 (2017) 92–100.
[42] S.L. Quane, J.K. Russell, L.A. Kennedy, A low-load, high-temperature deformation apparatus for volcanological studies, Am. Mineral. 89 (2004) 873–877.